

Supporting Information

Carbon Nanofiber Reinforced Strain Sensors with High Breathability and Anisotropic Sensitivity

Shuhua Peng,^{1*} Shuying Wu,² Yuyan Yu,¹ Zhao Sha,¹ Guang Li,¹ Trung Thien Hoang,³ Mai
Thanh Thai,³ Thanh Nho Do,³ Dewei Chu,⁴ and Chun H. Wang^{1*}

¹*School of Mechanical and Manufacturing Engineering, UNSW, Sydney, NSW 2052, Australia.*

²*School of Engineering, Macquarie University, Sydney, NSW 2109, Australia.*

³*Graduate School of Biomedical Engineering, UNSW, Sydney, NSW, 2052, Australia*

⁴*School of Materials and Science Engineering, UNSW, Sydney, NSW 2052, Australia.*

(Emails: shuhua.peng@unsw.edu.au; chun.h.wang@unsw.edu.au)

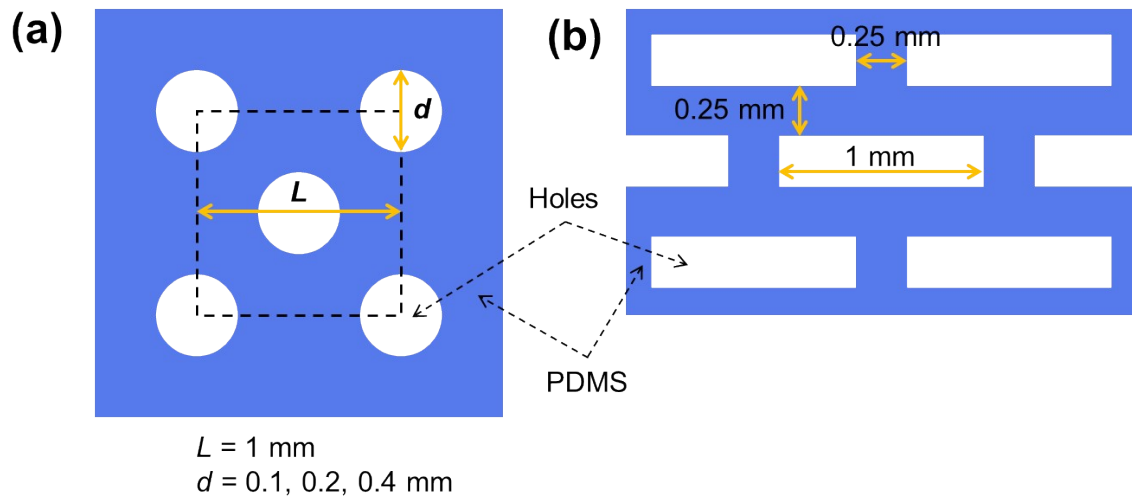


Fig. S1 Parameters for laser cutting to fabricate holey PDMS substrates. (a) Circular holes with constant distance between holes ($L = 1 \text{ mm}$) and three different diameters ($d = 0.1, 0.2$ and 0.4 mm); (b) Isotropic holey slots with aligned angle of 0° . The length of slots is 1 mm and the distance between slot edges is 0.25 mm .



Fig. S2 Commercially available breathable medical tape from 3M with porosity of ~ 5%.

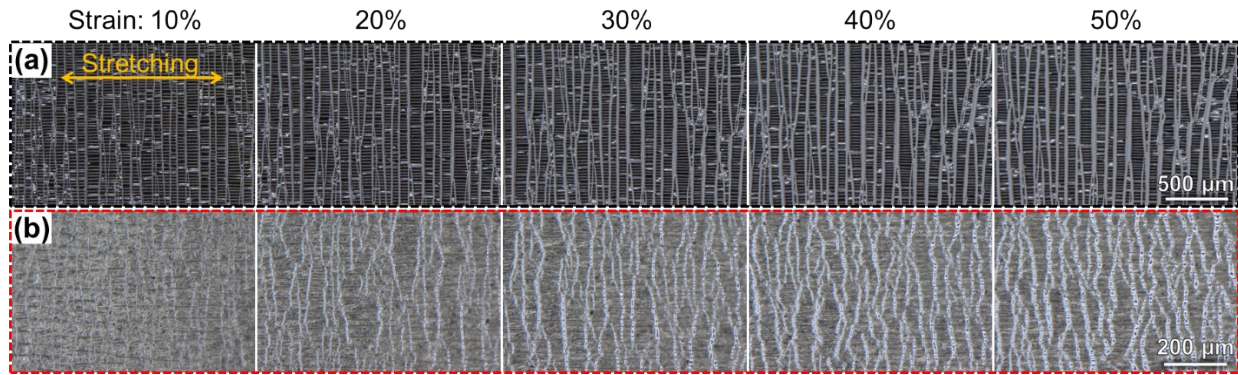


Fig. S3 Optical microscope images of the bare Pt coating (a) and CNFs reinforced Pt coating (b) on PDMS under stretching, respectively. The strain levels were indicated on top of the images.

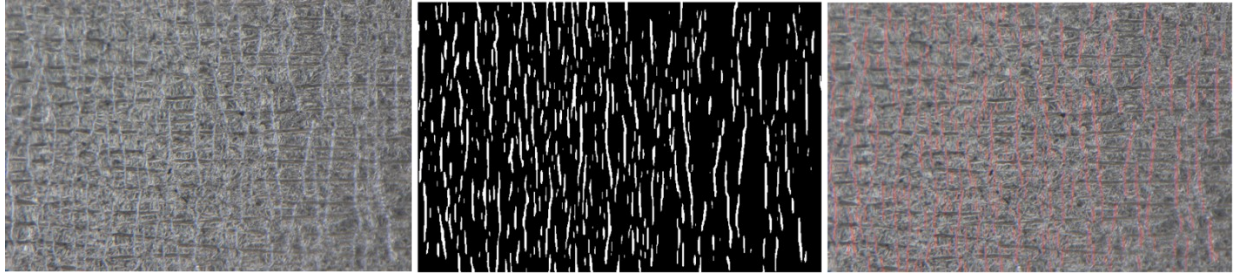


Fig. S4 An example of image analysis to extract the crack length and spacing from optical microscope image. A multi-step image processing was performed in view of extracting the cracked area from the optical images. Firstly, the color image was converted into a greyscale image, where the intensity of the image was adjusted to improve the contrast between the cracks and the background. Secondly, the crack-like structures were enhanced using multi-scale Hessian filtering techniques developed for angiographic images processing. The resulting image was then converted into a binary image, where blobs having an aspect ratio lower than 5 were excluded, i.e. only the elongated, crack-like structures were retained. The final image can then be compared with the initial colored images, demonstrating that the cracks are correctly identified. Afterwards, the crack information, such as the crack length and crack width can be extracted.

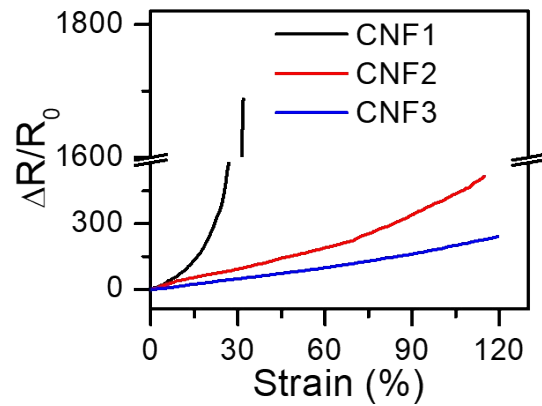


Fig. S5 Effect of areal weight of CNFs on the resistance change as a function of strain for strain sensors based on CNF/Pt coatings. The areal weights of CNFs were 0.25 (CNF1), 0.75 (CNF2) and 1.5 $\text{mg}\times\text{cm}^{-2}$ (CNF3), respectively. The thickness of Pt coating is 50 nm.

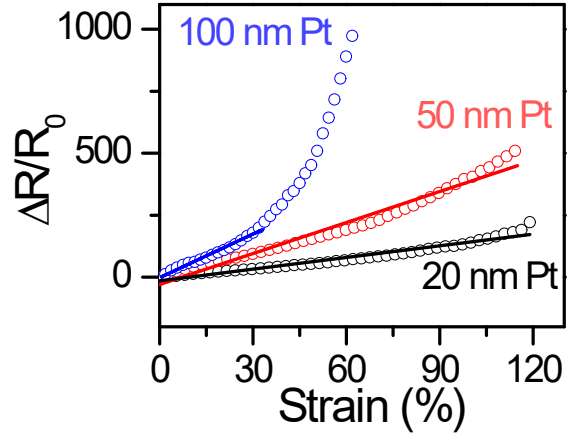


Fig. S6 Effect of Pt coating thickness on the resistance change as a function of strain for strain sensors based on CNF/Pt coatings. Three Pt thicknesses including 20, 50, and 100 nm were utilized. The areal weight of CNFs is $0.75 \text{ mg} \times \text{cm}^{-2}$. As for the strain sensors with different Pt coating thicknesses, their sensing performance in terms of their linear sensing range and GFs were 125% and 157 for 20 nm, 121% and 417 for 50 nm, and 37% and 587 for 100 nm, respectively. The strain sensor with 50 nm Pt coating combines both high sensitivity and wide linear sensing range and hence it is selected as the optimal condition for sensor fabrication.

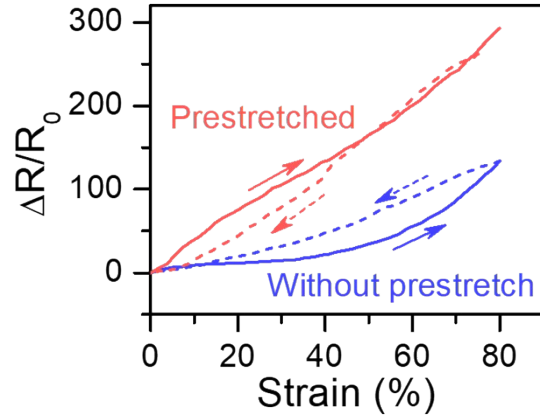


Fig. S7 Effect of prestretching on the sensing performance. The strain sensors were activated by prestretching to a strain of 100% before resistance measurements. The resistance changes as a function of strain became larger and more linear after prestretching. The areal weight of CNFs is $0.75 \text{ mg} \times \text{cm}^{-2}$ and the Pt thickness is 50 nm.

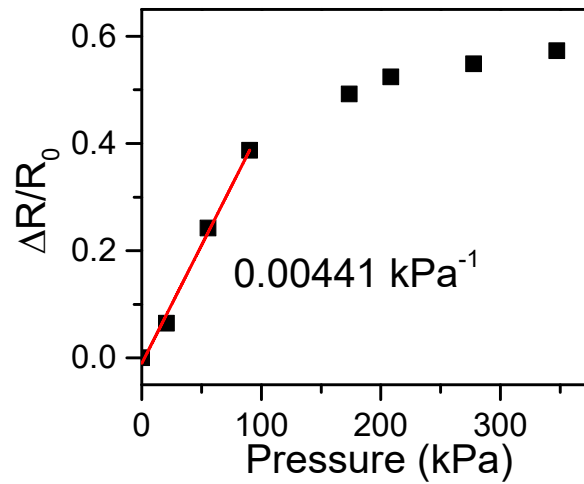


Fig. S8 Resistance changes as function of pressure for the strain sensor of Pt/CNFs.

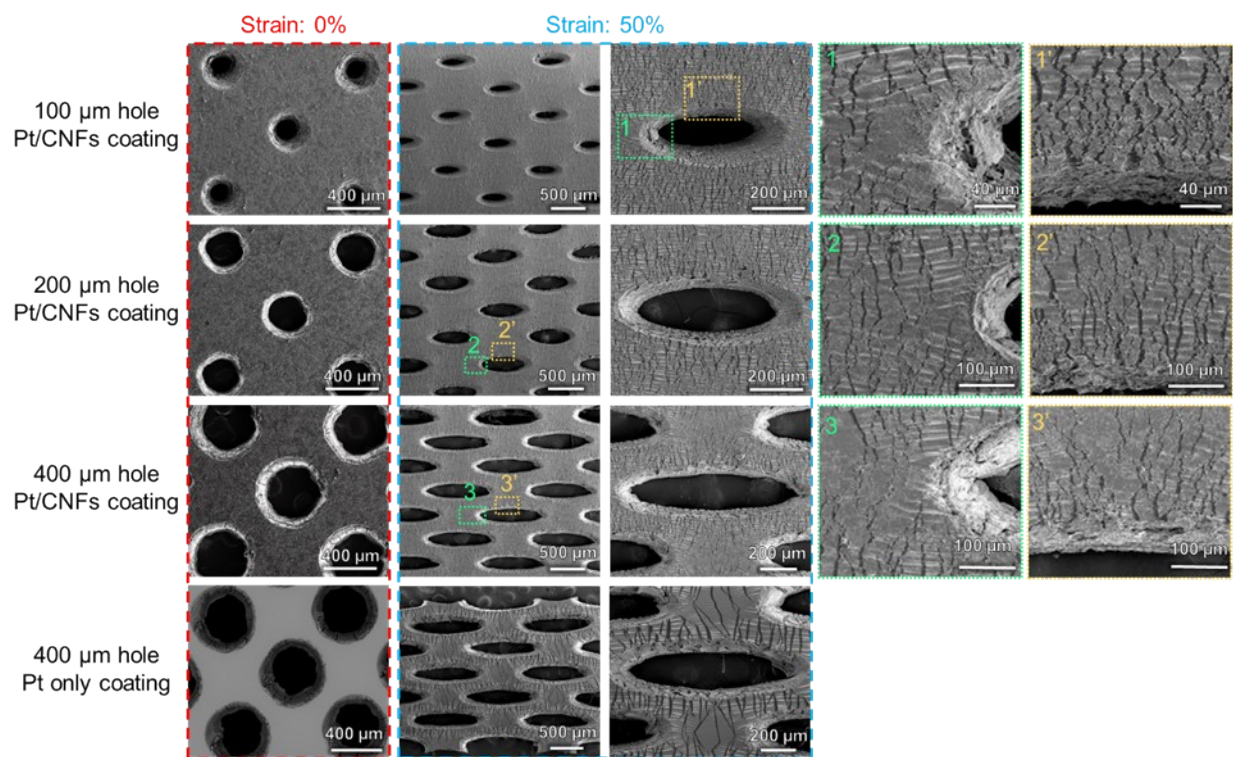


Fig. S9 SEM images of the breathable strain sensors with different hole diameters and conductive coatings. The hole diameter and the strain levels are indicated.

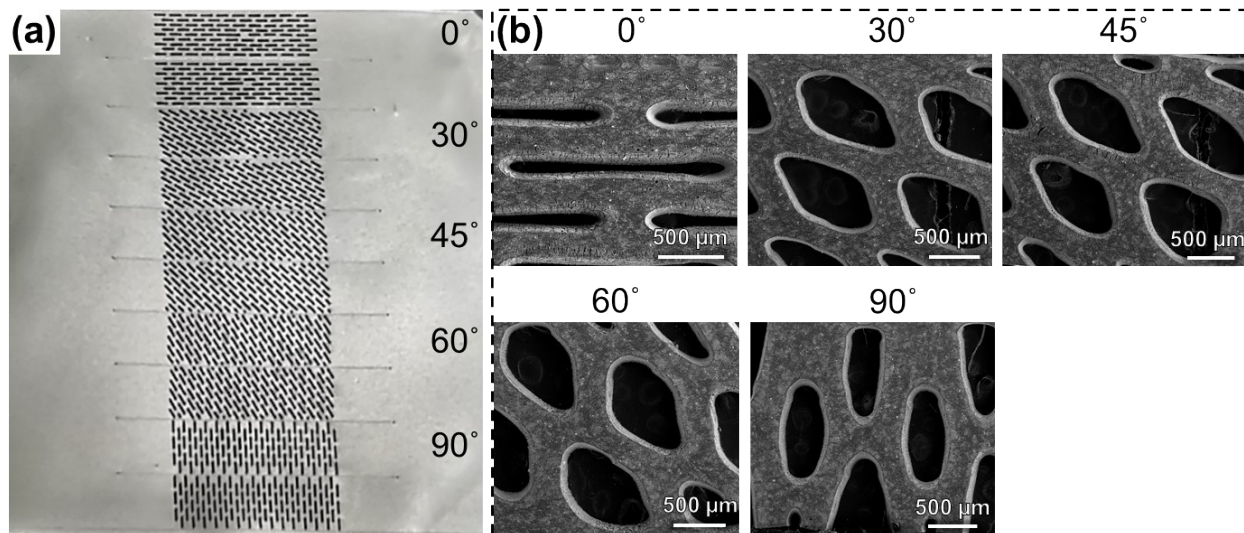


Fig. S10 Optical image (a) of anisotropic strain sensors based on aligned slots before stretching and corresponding SEM images (b) under strain of 50%. The aligned angles are indicated.

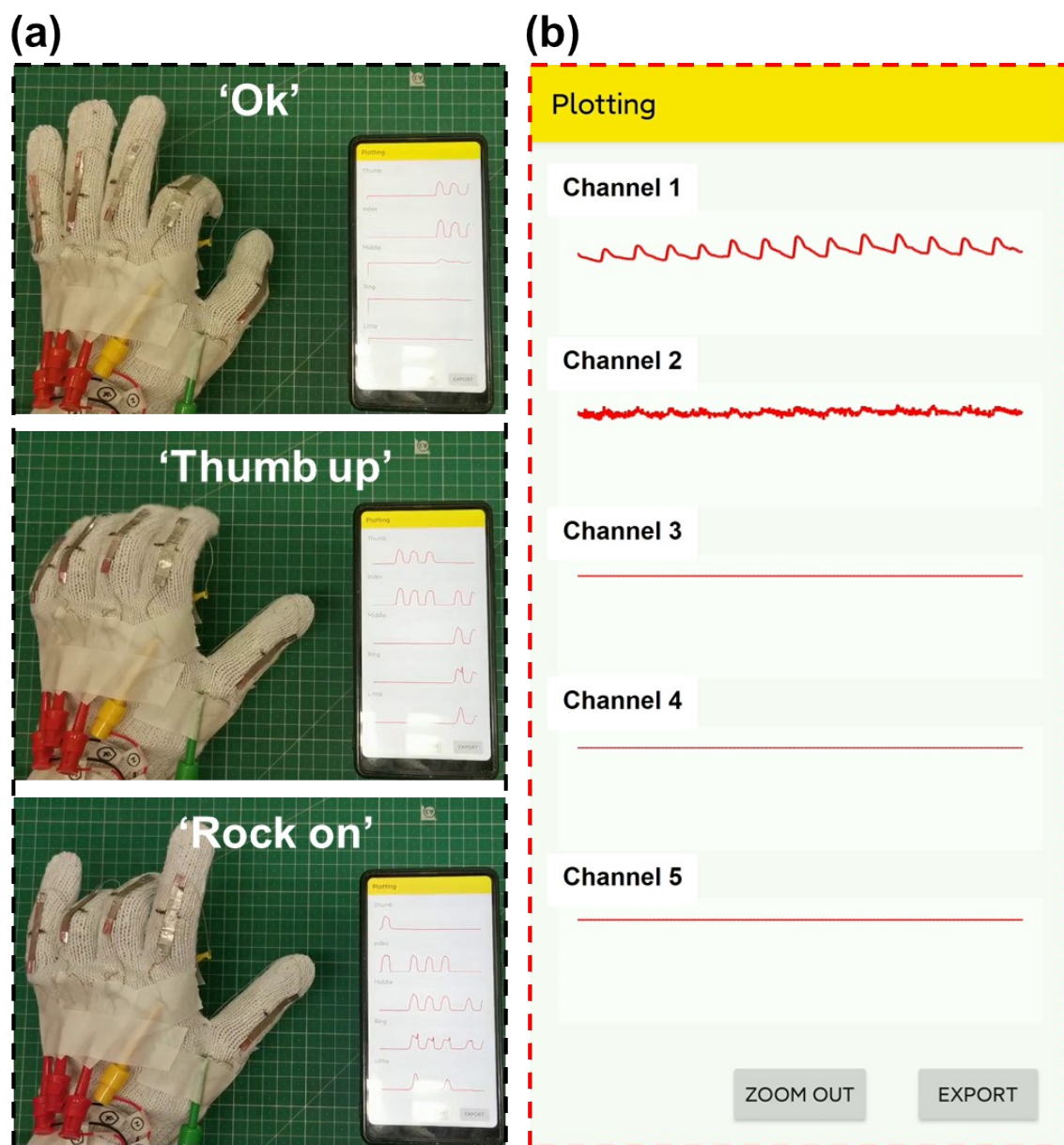


Fig. S11 (a) Screen shots of the resistance changes of smart glove responding to bending fingers associated with different hand gestures; (b) Screen shots of custom-developed mobile application to record the resistance changes induced by human wrist pulse. The strain sensor (200 μm diameter with Pt/CNFs coating) was mounted onto human wrist and connected to Channel 1 while Channels 2 to 5 were in the disconnected state.

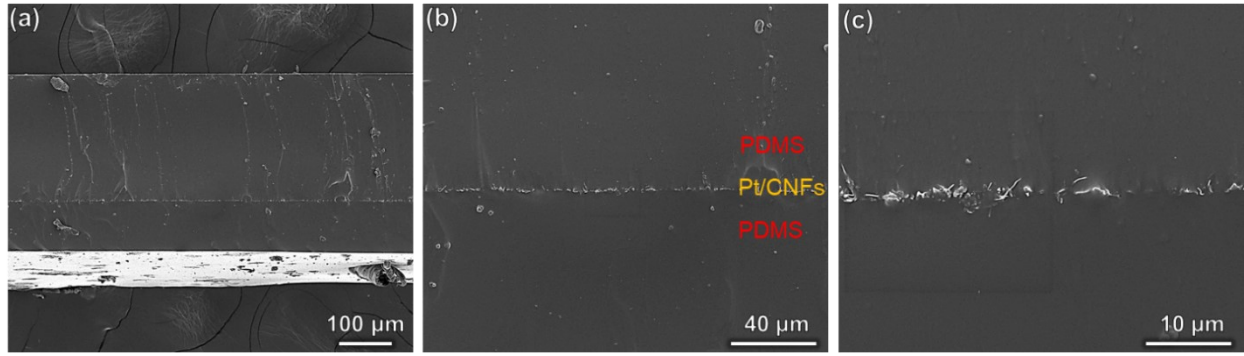


Fig. S12 SEM images of the cross-section view the three-layered microstructure of strain sensor under different magnifications.

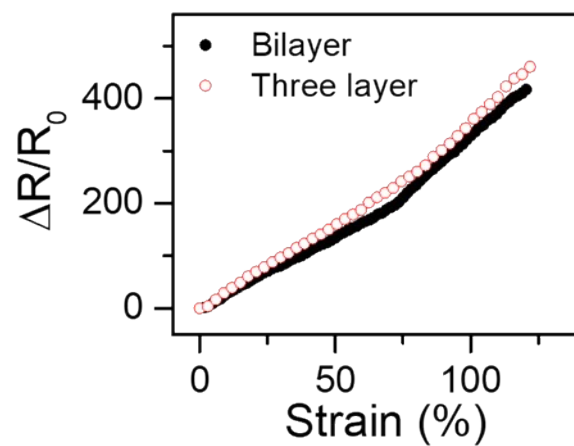


Fig. S13 The relative resistance changes as a function of strain for the strain sensors with bilayered PDMS/Pt and three-layered PDMS/Pt/PDMS.

Table 1. Comparison of sensing performance in terms of maximum sensing strain and gauge factor for previously reported strain sensors.

Strain sensors	Maximum sensing range	Gauge factor	Reference
Pt/CNFs/PDMS	121%	417	This work
Graphene aerogel/PDMS	19%	61.3	[1]
VGNs/PDMS	120%	32.6	[2]
Gold thin film on modified PDMS	50%	75.8	[3]
Gold thin film on PDMS	0.5%	200	[4]
PEDOT/CNFs/PDMS	47%	278	[5]
Fish scale-like rGO/tape film	82%	16.2	[6]
Hybrid AgNWs/AuNWs	5%	236	[7]
Graphene woven fabrics on PDMS	8%	500 at 2%	[8]
Graphene-nanocellulose paper/PDMS	100%	7.1	[9]
Fragmentized graphene foam/PDMS	70%	15	[10]
Compressed graphene foam/PDMS	120%	7.2	[11]
Aligned carbon nanofiber	30%	180	[12]
GO/AgNWs	10%	105	[13]
CNTs/PU	50%	111	[14]
CNTs/PDMS	175%	11	[15]
CNT bundles	70%	256	[16]
MXene-graphene composite	52.6%	190.8	[17]
AgNW/MXene fiber	15%	128	[18]
CNT/GO	100%	287.6	[19]

References

- [1] S. Wu, R.B. Ladani, J. Zhang, K. Ghorbani, X. Zhang, A.P. Mouritz, A.J. Kinloch, C.H. Wang, *ACS Appl. Mater. Interfaces*, **2016**, *8*, 24853.
- [2] S. Wu, S. Peng, Z.J. Han, H. Zhu, C.H. Wang, *ACS Appl. Mater. Interfaces*, **2018**, *10*, 36312.
- [3] S. Pan, Z. Liu, M. Wang, Y. Jiang, Y. Luo, C. Wan, D. Qi, C. Wang, X. Ge, X. Chen, *Adv. Mater.*, **2019**, *31*, 1903130.
- [4] T. Yang, X. Li, X. Jiang, S. Lin, J. Lao, J. Shi, Z. Zhen, Z. Li, H. Zhu, *Mater Horiz.*, **2016**, *3*, 248.
- [5] S. Peng, S. Wu, Y. Yu, P. Blanloeuil, C.H. Wang, *J. Mater. Chem. A*, **2020**, *8*, 20531.
- [6] Q. Liu, J. Chen, Y. Li, G. Shi, *ACS Nano*, **2016**, *10*, 7901.
- [7] M.D. Ho, Y. Ling, L.W. Yap, Y. Wang, D. Dong, Y. Zhao, W. Cheng, *Adv. Funct. Mater.*, **2017**, *27*, 1700845.
- [8] T. Yang, W. Wang, H. Zhang, X. Li, J. Shi, Y. He, Q. Zheng, Z. Li, H. Zhu, *ACS Nano*, **2015**, *9*, 10867.
- [9] C. Yan, J. Wang, W. Kang, M. Cui, X. Wang, C.Y. Foo, K.J. Chee, P.S. Lee, *Adv. Mater.*, **2014**, *26*, 2022.
- [10] Y.R. Jeong, H. Park, S.W. Jin, S.Y. Hong, S.-S. Lee, J.S. Ha, *Adv. Funct. Mater.*, **2015**, *25*, 4228.
- [11] Z. Zeng, S.I. Seyed Shahabadi, B. Che, Y. Zhang, C. Zhao, X. Lu, *Nanoscale*, **2017**, *9*, 17396.
- [12] J.-H. Lee, J. Kim, D. Liu, F. Guo, X. Shen, Q. Zheng, S. Jeon, J.-K. Kim, *Adv. Funct. Mater.*, **2019**, *29*, 1901623.
- [13] Y. Liu, X. Shi, S. Liu, H. Li, H. Zhang, C. Wang, J. Liang, Y. Chen, *Nano Energy*, **2019**, *63*, 103898.
- [14] H. Sun, K. Dai, W. Zhai, Y. Zhou, J. Li, G. Zheng, B. Li, C. Liu, C. Shen, *ACS Appl. Mater. Interfaces*, **2019**, *11*, 36052.
- [15] P. Wang, W. Wei, Z. Li, W. Duan, H. Han, Q. Xie, *J. Mater. Chem. A*, **2020**, *8*, 3509.
- [16] J. Lee, S. Pyo, D.-S. Kwon, E. Jo, W. Kim, J. Kim, *Small*, **2019**, *15*, 1805120.
- [17] Y. Yang, Z. Cao, P. He, L. Shi, G. Ding, R. Wang, J. Sun, *Nano Energy*, **2019**, *66*, 104134.
- [18] J.-H. Pu, X. Zhao, X.-J. Zha, L. Bai, K. Ke, R.-Y. Bao, Z.-Y. Liu, M.-B. Yang, W. Yang, *J. Mater. Chem. A*, **2019**, *7*, 15913.
- [19] H. Zhang, D. Liu, J.-H. Lee, H. Chen, E. Kim, X. Shen, Q. Zheng, J. Yang, J.-K. Kim, *Nano-Micro Lett.*, **2021**, *13*, 122.